Hydrokinetic Optimization of Commercial Scale Slurry Bubble Column Reactor

Wayne Strasser
Eastman Chemical Company, Kingsport, TN 37662

Alan Wonders
Westlake Chemical Company, Longview, TX 75602

DOI 10.1002/aic.12629
Published online April 27, 2011 in Wiley Online Library (wileyonlinelibrary.com).

An in-depth numerical study has been carried out to investigate a high-pressure commercial scale (2–8 m diameter, 30–40 m in height) slurry bubble column reactor. Typical superficial gas velocities are in the range of 0.5–3 m/s, and overall vapor holdups are in the range of 0.45–0.85. The study revealed that steady compartmental reaction models do not match plant data when reaction time constants are fast. Also, off-the-shelf commercial computational fluid dynamics codes do not produce useful information about a reactive column of this scale without first validating the model using data "anchors" from full-scale operational columns. Important measures include both transient and time-averaged profiles, integrals, and extrema of vapor holdup and reactants. Reactor designs based on this study show both improved productivity and product quality, allowing record production from existing plants along with substantial capital scope reduction for new plants. © 2011 American Institute of Chemical Engineers
AIChE J, 58: 946–956, 2012
Keywords: computational fluid dynamics, bubble columns, multiphase flow

Introduction

The liquid-phase partial oxidation of *para*-xylene (pX) to terephthalic acid (TPA) is conducted at very large commercial scales, principally for providing raw material for polyester fiber and packaging products. Relatively large oxidation reactors provide individual capacities presently ranging from 60,000 to 120,000 kg/s of TPA for new construction. Although the partial oxidation of pX to TPA proceeds at very high yields and purities, further small improvements have significant impact due to scale. The overall stoichiometry of TPA production is deceptively simple, as shown in Eq. 1.

$$\mathrm{pX} + 3\mathrm{O_2} = \mathrm{TPA} + 2\mathrm{H_2O} \quad (1)$$

Correspondence concerning this article should be addressed to W. Strasser at strasser@eastman.com.

Behind the seemingly simple overall reaction equation, there are at least four principal reaction steps, and each of those steps involves several elementary reaction substeps. Various by-products affect the TPA product's fitness for use differently, while some are important at concentrations as low as 1 ppm by weight.

Broadly speaking, undesirable reactions are suppressed by higher concentrations of dissolved oxygen and are promoted by higher concentrations of dissolved aromatic species. To elevate the concentration of dissolved oxygen, it is desirable to maximize aeration of the reaction medium, promoting mass transfer from gas to liquid phase. Notably, the reaction proceeds with such intensity that the average survival time of an oxygen molecule after dissolving is only a few seconds. Thus, the local concentration of oxygen in the gas phase varies greatly depending on the agitation and location of gas feeding. Also, the concentration of dissolved oxygen involves a competition between dissolution rate and chemical demand.

Similarly, the local concentration of pX will vary according to agitation and the location of pX addition. To lower the peak concentration of dissolved aromatics, it is desirable to mix off the feed plume of pX quickly. However, the interplay of dissolved oxygen and dissolved aromatic is very complex. Different aromatic intermediate species react at different rates and with different stabilities while "searching" for an oxygen molecule. An ideal reaction system would have the reactants' availabilities matched with their demands on an instantaneous basis. Important interactions exist when optimizing local oxygen and local aromatic concentrations. As a result, one of the goals in improving on this rich, well-established method of making TPA is to optimize methods of gas and liquid feeding. Disclosures of the current invention can be found in US Patents 7,371,894, 7,381,836, 7,390,921, 7,399,882, 7,482,482, 7,495,125, 7,498,002, 7,498,003, 7,507,857, 7,563,926, 7,572,932, 7,572,936, 7,589,231, 7,608,733, 7,659,427, 7,692,036, 7,692,037, and 7,741,515, all of which are titled, "Optimized liquid-phase oxidization." A typical arrangement of an oxidation bubble column is given in Figure 1. The larger diameter feed plenum at the bottom is the octagonal multiholed air sparger, while the smaller diameter system in the middle of the column is a liquid phase reactant distributor and the associated support systems.

For the production scales involved in this study, the typical method of agitation involves a mechanical agitator with purchased costs far exceeding 1 million USD. It is preferred in the present research that the agitation work is provided by rising gas plumes in a bubble column. Although the experimental and computational work for bubble columns has historically been staggering, nothing apparently exists for the conditions of this work:

- high pressure (0.3–3 MPa);
- high superficial gas velocity and holdup (0.5–3 m/s, 0.45–0.85);
- high content of solids (8–45% of the total slurry weight);
- strong evaporation (>30% of the gas fed by mass at operating temperatures as high as 250°C);
- large diameter (2–8 m and 30–40 m in height);
- fast reaction kinetics (pseudo half-lives of some species under 10 s).

The most recent hydrodynamic work that comes near the conditions in this work is that of Nottenkamper et al.[1] with superficial velocities approaching 1.5 m/s in a 1.0-m diameter column at atmospheric pressure. They showed liquid centerline velocities near 2.0 m/s, with centerline holdups approaching 0.8. They found near-linear positively sloped axial holdup profiles, with the slope staying about the same (excluding the bottom transition region) with increasing superficial velocity. A near-linear hydrostatic pressure profile resulted from all the column chaos. As it is known that pressure strongly affects bubble size population,[2] and as the other evaporative, chemical, and solids issues are absent, the results of the Nottenkamper study can only be used as a guide.

Effect of pressure, temperature, and solids

Although not directly related to this work, there have been many valuable works that give insight about pertinent physics. For a much smaller column and slightly lower superficial gas velocities, Lou et al.[3] described the effects of pressure and concentration of solids. They found that higher pressures lead to higher holdups (from smaller bubbles), with the pressure effect being more pronounced at higher concentrations of solids. The authors proposed that Rayleigh–Taylor and Kelvin–Helmholtz instabilities, alone, were not the cause of reduced bubble size. They offered a mechanism by which internal bubble centrifugal forces become strong relative to surface tension forces at higher gas densities. Also, large bubbles attract smaller bubbles in their wakes. Finally, they found that the presence of solids raised the overall bubble size.

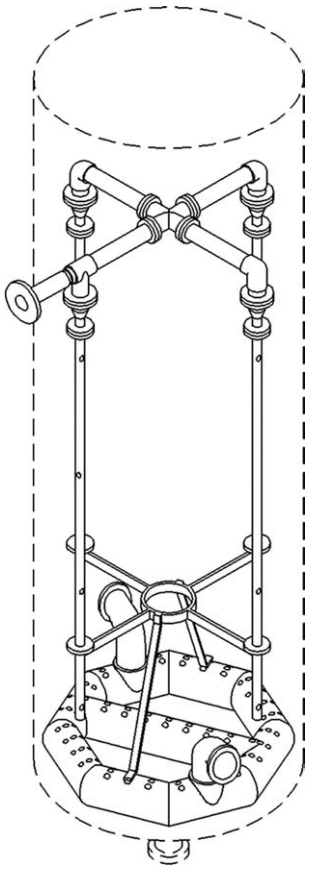

Figure 1. Typical arrangement of the lower section of an oxidation bubble column.

It was reported in a later publication by Yang et al.[4] that a three-phase bed (large particle) internal heat transfer coefficient increased with pressure and reached a maximum at around 6– 8 MPa (and decreased above this), but the opposite occurs for a bubble column (small particle). The pressure effects on heat transfer coefficient in a bubble column are a result of multiple competing physics issues: higher overall circulatory motion with larger bubbles, more energy dissipation in the wake of larger bubbles, liquid viscosity increasing with pressure, surface tension decreasing with pressure, and the increase in bubble passage frequency at higher pressures. As with Lou et al.,[3] this work involved a small column and a lower gas superficial velocity than that of this work. Their results echo those of their earlier

colleagues who found a larger bubble size and higher heat transfer coefficient with increasing concentration of solids. One might estimate that the effects of solids on the heat transfer coefficient would depend on local turbulence augmentation or suppression resulting from the addition of the dispersed solid phase (Strasser[5]). Solids affected the system more noticeably at ambient pressures due to the relatively large bubble sizes at the lower pressures. Temperature increases were found to increase the heat transfer coefficient, mainly caused by the decrease in liquid viscosity. Lau et al.[6] studied the effect of pressure, temperature, and column size on the mass transfer coefficient, k_La, which includes the effect of interfacial area per volume of reaction mixture. It was found, using a continuous stirred tank reactor (CSTR) model, that k_La increased with increasing pressure, increasing temperature, and decreasing column size (mainly due to an increased holdup by a reduced circulation rate). The authors include a vast list of prior studies of mass transfer coefficients in ambient bubble columns. Similar directional temperature and pressure effects on k_La were concluded by Jin et al.[7] In addition, a decreasing k_La was discovered as loading of solids increased. This confirms other researchers' findings about the reduction of bubble size with increased levels of solids.

Scale-up

The challenge of bubble column scale-up has been addressed by a number of authors. An early review paper by Rosen and Krylov[8] proposed the fact that the difficulty of moving from laboratory to industrial scale is related mainly to phase velocity distributions. Even in cases involving the same mean velocity, local issues, such as bypassing, can create major differences at varying equipment scales. Increasing scale increases Reynolds number, which improves lateral mixing and decreases local concentration driving forces. They indicate than an effective means of scaling equipment would be to consider the mass transfer efficiency, which is proportional to a superficial velocity scale. Important at any scale, in most cases, would be to have a uniform velocity distribution. The concepts are further expounded on by Deckwer and Schumpe[9] who showed k_La to be proportional to gas superficial velocity to the 0.7 power and to column diameter to the 0.17 power, but only for small columns (diameter < 0.6 m). The liquid mixing time was found to depend on diameter to the 4/3 power, while gas mixing time depended on column diameter to the 3/2 power; however, the gas mixing time dependency was highlighted as questionable given the substantial spread in available data. Similarly, Zlokarnik[10] showed k_La proportional to a velocity scale and liquid mixing time proportional to diameter to the 3/2 power.

An in-depth discussion on scale-up issues was authored by Martin et al.[11] They reported that column diameter only affects the gas holdup below superficial velocities of 0.08 m/s and that $k_L a/r_g$ is constant with diameter above this. They studied various behaviors, using a relatively small column and a peak superficial gas velocity of 0.005 m/s (homogeneous regime), and cast everything in the form of $k_1 a = \psi u_g^{\beta}$. The power β, related to the effectiveness of the power input at creating interfacial area (balance between coalescence and breakup), varied from 0.35 to 1.1. No effect of column scale on β was found. The constant ψ, on the other hand, was more of a measure of mean bubble size and how the mean size is affected by liquid properties. As a result, ψ decreased with increasing column diameter and increasing liquid viscosity. At the same time, liquid viscosity also reduces β. It was said that to scale up gas distribution devices, one needs to either maintain gas superficial velocity or Froude number. The scalable region in their work included up to column diameters of 6 m. Both Zlokarnik[10] and Martin et al.[11] noted that chemical reactions further complicate the considerations.

Method

Overall physics

Numerical methods for investigating bubble columns have been a subject of intense study for years. An axial dispersion approach was used by Xie and Li[12] to study pX oxidation. A 151-page review of various numerical approaches was given by Rafique et al.[13] It was found through internal evaluations at Eastman Chemical Company that axial dispersion and compartmental approaches do not produce chemical species profiles for pX oxidation like those actually measured in a commercial scale unit. The results of a steady compartmental model (with the average of local fluctuations superimposed onto the mean) are superior to an axial dispersion model, but still apparently distort the transient effects of correlated hydrodynamics and chemistry. As a result, a fully transient 3-D hydrokinetic Eulerian–Eulerian three-phase computational fluid dynamics (CFD) approach is sought. Each phase is allowed separate velocity, turbulence, thermal, and chemical fields but share a common pressure. The liquid is assumed to be everywhere continuous, while the compressible gas and solid phases are assumed to be everywhere dispersed. Provisions are made for areas in which the gas holdup approaches unity. Continuity for phase α is shown below in Eq. 2.

$$\frac{\partial r_\alpha \rho_\alpha}{\partial t} + \frac{\partial r_\alpha \rho_\alpha u_{\alpha j}}{\partial x_j} = 0 \tag{2}$$

Here, r is the volume fraction of phase α, ρ is its density, u is its velocity component in direction j, and t is time. The Reynolds-averaged linear momentum balance in Cartesian coordinates for a compressible phase α is shown in Eq. 3 after invoking the Stokes assumption.

$$\frac{\partial r_\alpha \rho_\alpha u_{\alpha i}}{\partial t} + \frac{\partial r_\alpha \rho_\alpha u_{\alpha i} u_{\alpha j}}{\partial x_j} = \frac{\partial}{\partial x_j} r_\alpha \left[\mu_\alpha \left(\frac{\partial u_{\alpha i}}{\partial x_j} + \frac{\partial u_{\alpha j}}{\partial x_i} - \frac{2}{3} \delta_{ij} \frac{\partial u_{\alpha k}}{\partial x_k} \right) - \rho_\alpha \left\langle u'_{\alpha i} u'_{\alpha j} \right\rangle \right] - r_\alpha \frac{\partial p}{\partial x_i} + r_\alpha (\rho_\alpha - \rho_{\text{ref}}) g_i + S_{\alpha i} + M_{\alpha i} \tag{3}$$

The phase α viscosity is given by μ, δ is the Kronecker Delta, p is pressure, g is gravity, and u' is a fluctuating velocity component. The term $\left\langle u'_{\alpha i} u'_{\alpha j} \right\rangle$ is the Reynolds stress tensor. Of course, the liquid phase and solid phases are incompressible; therefore, the div (normal stress) term drops out of the right-hand side of Eq. 3 for the liquid and solid

phases and remains for the vapor phase. $S_{\alpha i}$ involves momentum sources due to evaporation and condensation, while $M_{\alpha i}$ includes interfacial forces (drag and nondrag).

The shear stress transport (SST) two-equation linear eddy viscosity model of Menter[14] is used for computing the Reynolds stress terms for the continuous phase. This model involves a smooth blend between the standard k–ε model of Launder and Spalding[15] in the freestream and the k–ω model of Wilcox[16] near the wall. Here, k is the turbulence kinetic energy, ε is the turbulence dissipation rate, and ω is the specific dissipation rate. In the SST model, additional consideration is given to the transport of the principal turbulent shear stress via (1) an eddy viscosity limiting function and (2) a cross-diffusion term in the transport equation for ω. Also, there is a turbulence production limiter, as discussed in the ANSYS Solver Documentation,[17] preventing the artificial build-up of fluctuating velocity in regions of irrotational strain. The local eddy viscosities of the dispersed phases are functions of the eddy viscosity of the continuous phase. "Scalable" wall functions, discussed in ANSYS Solver Documentation,[17] are an alternative to standard wall functions of Launder and Spalding.[15] They have the advantage of being less sensitive to variation in near-wall grid resolution throughout the domain. The distance from the wall is computed via a Poisson equation with a uniform source value of -1. Additional compressibility effects and buoyancy-driven turbulence have been neglected in this work. That is to say that the effects of the violent, buoyancy-driven shear layer production in the erupting bubble column are included in the equations and dominate the turbulence sources/sinks, but the additional production and dissipation terms due to the occasional alignment of the gravity vector with the local pressure gradient in the k and ω equations have not been included. The latter effects are less certain, and the constant coefficient on the dissipation transport equation term is derived from 2-D low Reynolds number natural convection.[17] As with most Reynolds-averaged turbulence models, the boundary layers are considered everywhere turbulent. The profiles in the near-wall bubbly region is a topic of current debate. For example, Vitankar et al.[18] discusses boundary layer thinning by increased turbulence in two-phase flow, so there is not an obvious answer to the near-wall approach that is best. More complete discussions of turbulence models, advantages, and caveats are available in the study of Pope.[19] It is well-known that eddy viscosity turbulence computations are limited. For the purposes of industrial bubble column design optimization, it was decided that the use of a linear two-equation model for the liquid phase and a zero-equation model for the dispersed phases was an adequate starting point. As will be discussed in an upcoming section, the momentum balance (obviously includes phasic turbulence) is a result of many forces. It is the tuning of these to match experimental information that is key. The results shown in this article represent a very small subset of the actual design work; time did not permit the use of a Reynolds stress model and certainly not a large eddy simulation approach.

The phasic chemical species balance is shown in Eq. 4:

$$\frac{\partial r_\alpha \rho_\alpha \phi_\alpha}{\partial t} + \frac{\partial r_\alpha \rho_\alpha u_{\alpha j} \phi_\alpha}{\partial x_j} = \frac{\partial}{\partial x_j} r_\alpha \left[\left(\rho_\alpha D_\alpha^\phi + \frac{\mu_{t,\alpha}}{Sc_{t,\alpha}} \right) \frac{\partial \phi_\alpha}{\partial x_j} \right] + R_\alpha^\phi \tag{4}$$

The gradient diffusion hypothesis has already been invoked to separate out the molecular and turbulent diffusive effects on the right-hand side, where μ_t is the turbulent viscosity. $R_{\alpha\Phi}$ is simply the reactive species volumetric source terms for species Φ in phase α. The basis for $R_{\alpha\Phi}$ is Eq. 1 plus enough competing, parallel reactions and species to account for the preponderance of oxidant consumption. D is the component diffusivity, and Sc_t is the turbulent Schmidt number. When viscous heating and compression work are ignored, the phasic energy equation looks very similar to Eq. 4 with the appropriate substitutions. Extremely large bulk evaporation rates are handled through appropriate sources and sink terms similar to those in Eq. 3.

Drag, bubble size, and other forces

The momentum balance within the bubble column results in various important production rate-controlling overall characteristics. These include vapor holdup, overall backmixing, local species mixing rates, and local velocity profiles. A local cell momentum balance is directly related to the joint effects of:

- drag coefficient (including bubble swarm effects);
- bubble size distribution;
- bubble-induced turbulence;
- turbulent dispersion;
- turbulence stress closure; and
- nondrag forces, such as lift and virtual mass.

A given balance can be achieved from various combinations of these. Some of the most recent bubble swarm drag relationship work is given by Simonnet et al.[20] but deals with a situation unlike that of this work. It is valid for atmospheric pressure, air/water, a maximum bubble diameter of 10 mm, and local void fractions less than 30%. A recent study of turbulence closure and interfacial forces is carried out by Zhang et al.[21] They proposed combinations of methods that produce more realistic validations but all for homogenous flow. Monohan et al.[22] studied the momentum balance for heterogeneous flow, and they found that large diameter column heterogeneous flow is not observed without considering bubble coalescence. Treating the gas phase as two general classes of bubbles, small and large, was explored by Krishna and Ellenberger.[23] A relatively new interfacial area transport equation which replaces the typical simple algebraic definition has recently been proposed by Ishii.[24] Interactions between the phases typically include bubble-induced turbulence (from Sato[25]) and turbulent dispersion (from Lopez de Bertodano[26]).

Bubble size prediction methods

The physical phenomena which govern bubble coalescence and breakup have been considered by many authors since the 1960s. Wilkinson et al.[27] summarized the number of older works and discussed the fundamental elements of breakup. They showed that, for large bubbles, the stable bubble size is lower for a lower surface tension and lower viscosity. It is noted that the same surface tension trend applies to droplets (see also Strasser, Ref. 28), but that the critical Weber number is lower for droplets than for bubbles. The cause of this relates to the difference in the densities of the

dispersed phase and the continuous phase. Higher gas densities lead to higher breakup rates. The authors show that the formation of a neck is not a sufficient condition for breakup to occur. The density effect is manifested in the suction pressure resulting from the creation of a neck, that is, higher densities lead to more suction through the simple Bernoulli relation.

Later, an experimental study by Poherecki et al.[29] in a relatively small column (0.3 m diameter) and a maximum superficial gas velocity of 0.055 m/s revealed a lack of dependence of temperature, pressure, and air sparger geometry on the mean bubble size. They showed the fact that many correlations did not predict what they found experimentally. Surprisingly, a very simplified version of the well-known Prince and Blanch[30] model, in which a monodisperse bubble class with equal coalescence and breakup rates, gave a better estimate of bubble size.

A thorough comparison between four different models (Lehr et al.,[31] Luo and Svendsen,[32] and Prince and Blanch[30]) for coalescence and breakup was given by Wang et al.[33] All coalescence rates are expressed in terms of collision frequency multiplied by coalescence efficiency. Below is an outline of what the various models included:

- Prince and Blanch[30]
  - ○ Coalescence by turbulent collisions, buoyancy-driven collisions, and laminar shear collisions.
  - ○ Collision efficiency set by liquid film thinning.
  - ○ Breakup caused by collisions of structures of sizes equal to or smaller than the bubbles and excluded daughter bubble size distributions.
- Luo and Svendsen[32]
  - ○ Coalescence by turbulence collisions.
  - ○ Collision efficiency considered virtual mass and Weber number.
  - ○ Breakup involved theories of isotropic turbulence and probability and included daughter size distributions.
- Lehr et al.[31]
  - ○ Coalescence by turbulence collisions and different rise velocities.
  - ○ Breakup similar to that of Luo and Svendsen,[32] except that they assumed by a capillary constraint that interfacial and inertial forces balanced one another.
- Wang et al.[33]
  - ○ Coalescence by turbulent collisions, wake entrainment, and different rise velocities with a correction for local gas void fraction in the turbulent collisions formulation. They claim this is critical for the success of their model.
  - ○ Breakup due to turbulent eddies and large bubble wake instabilities including daughter size distributions.

The authors depicted a relatively close match in breakup rates to the experimental data by their model and that of Lehr et al.[31], noting that the Prince and Blanch[30] method led to over prediction of breakup rates caused by a self-sustaining near- unity value of breakup efficiency. They showed their model and that of Lehr et al.[31] produced M-shaped daughter size distributions, but that the Lehr et al.[31] model had an incorrect singularity at the center of the distribution. Generally, for low gas void fractions when coalescence dominates, the Prince and Blanch[30] and Lehr et al.[31] models underpredicted the bubble size, while the Luo and Svendsen[32] model predicted a disproportionate amount of both very large and very small bubbles. At higher void fractions (still low compared to this work), the results were similar except that the results of Lehr et al.[31] were closer to those of Wang et al.[33] Finally, the authors considered the models' ability to predict the transition from the homogeneous to heterogeneous regime. Both the models of Prince and Blanch[30] and Luo and Svendsen[32] failed to predict the transition and showed a decrease in bubble size with increasing gas feed rate. The other two models transitioned, but the Lehr et al.[31] model computed an unreasonably low volume fraction of bubbles of intermediate size. It should be mentioned that the above conclusions are limited in scope by choices of drag coefficients, turbulence modulation, and other CFD coupling issues.

Detailed surface contamination effects on bubble size distribution and mass transfer rates were studied by Martin et al.[34] at superficial gas velocities in the range of 0.0075–0.035 m/s. The Prince and Blanch[30] population balance model (PBM) approach was used along with the assumption that a bubble breaks up into two equally sized daughter bubbles. The addition of surface active species affects the behavior of single bubbles and swarms of bubbles in various, sometimes opposing, ways. Hydrodynamics and local mass transfer phenomena are modified by changes in properties and bubble swarm behavior. Bubble swarms do not behave like individual bubbles, in terms of mass transfer, so a 0.4 correction factor is applied onto the mass transfer coefficient for swarms. The authors isolated the effects of fluid properties from the effects of surface mobility, draining time, etc. For the evaluations of fluid properties, they found an agreement with theory that neither liquid density nor surface tension modified the critical Weber number. As the critical Weber number is lowered, fully mobile mass transfer expressions were simply changed to incorporate more bubbles in the column. For the surfactant effect evaluations, the work was broken into two categories: partially covered (surface coverage, Se, between 0 and 1) and full covered. In both cases, hydrodynamic effects were condensed into a single parameter, critical Weber number. Linear correlations of critical Weber number with ionic strength were proposed. Each had a negative slope and *y*-intercept near the air–water value of five, with the partially covered surface responding to strength more significantly. In other words, the size of the bubble populations was reduced (and presumably mass transfer was improved) in all cases by the addition of surfactant, but it was noted that more work is to be done to consider the effects of ion size.

Despite the rich background in methods development offered in the literature, application of commercial methods (implementations of PBM for CFX® (CFX) and Fluent® (FLUENT) are discussed in Olmos et al.,[35] and Chen et al.,[36] respectively) to pX oxidation proved ineffective at matching experimental holdup and velocity distributions and pressure fluctuations. Therefore, the authors have developed a novel population balance method for realistic industrial pX oxidation conditions. Without matching experimental hydrodynamic information, there is little hope of ascertaining the overall operating quality of various design configurations. The primary "tuning" that took place involved the bubble population balance method. Particular choices of models and

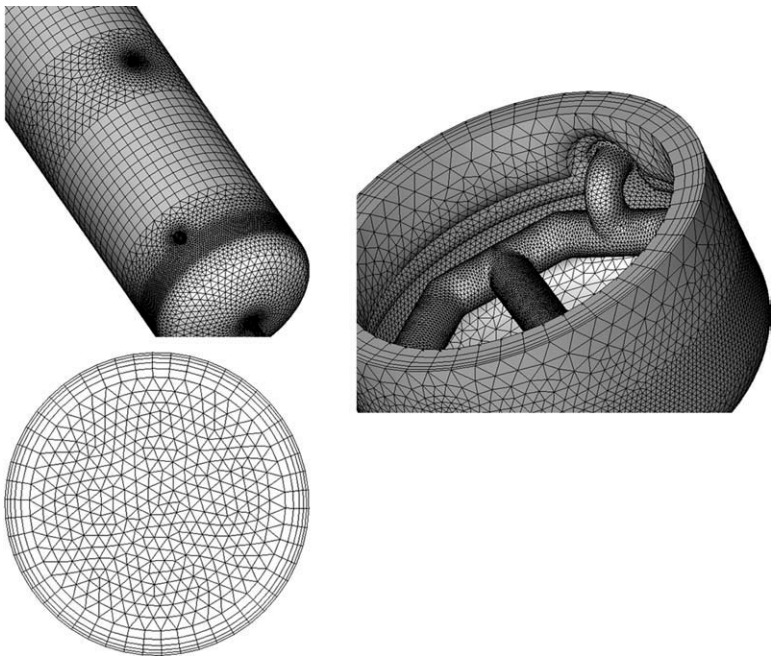

Figure 2. Some features of the computational mesh, specifically the cross-section in the bulk of the column, the outer walls, and the boundary layer inflation around the air sparger region.

coefficients have not been disclosed for this work due to the proprietary and unique nature of the liquid-phase oxidization at these conditions; however, it can be insightful to consider a relatively simple approach to assign the bubble size as a function of geometric position with the smallest bubbles near the sparger. Tuning involves changing the slopes of position functions, transition points, and bubble size extrema. Overall, the sizes in a typical model ranged from 0.005 to 0.2 m in diameter. While it is clear that bubble shapes and sizes change in space and time, methods like this have proven useful in this work.

Solver

The ANSYS CFX Release 11 solver (details and individual references found in the ANSYS Solver Documentation[17]) discretizes Eqs. 2–4 using a vertex-based finite volume method. Each term is converted to mesh element volume integrals and element surface integrals. Advection terms are discretized using a high-resolution algorithm similar to that of Barth and Jesperson. Time derivatives are discretized using a second-order transient scheme. Mass flows are discretized using a Rhie-Chow approach, modified by Majumdar, to avoid pressure decoupling on the colocated grid. The mass flow discretization also involves a Newton–Raphson linearization to handle compressibility effects. Viscous stresses, diffusion terms, and the pressure gradient are discretized using finite element shape functions, whose construction depends on the mesh element type. The solution algorithm is fully implicit, with velocity and pressure coupled together in the same matrix. The resulting system of equations is solved using a coupled incomplete lower upper (ILU) algebraic multigrid technique.

Mesh

The computational mesh, involving prisms, tetrahedra, hexahedra, and pyramids, was built in Gambit and TGRID®, with the intent to balance computational load and accuracy. The smallest grid length scales were near the various feeds, such as the gas sparger holes. The expansion (in all three dimensions) of cells away from the feeds to areas with lesser gradients was carried out in such a way so as to minimize cell aspect ratios, centroid shifts, and skewness. A "superblock" technique is used to ensure that the cells at block boundaries (including boundary layer blocks) meet each other with nearly uniform mesh spacing. More on these concepts can be found in the transonic gas turbine blade passage research of Strasser et al.[37] Also, the effects of gridding methods on the computational results are explored in the study of Strasser.[38] Typical total cell counts ranged from 100,000 to 1,000,000 cells, depending on the complexity of the feeds. Three features of the mesh are depicted in Figure 2. The upper-most picture shows the exterior mesh of the column. Higher mesh density is evident in the regions where nozzles penetrate the vessel walls. Outside of these regions, structured grid is used as much as possible, ensuring minimal false diffusion Strasser.[38] The lower left-hand part of Figure 2 shows a typical cross-section. Triangular mesh is extruded vertically, and a boundary layer is imparted near the wall. Finally, the bottom right-hand corner shows the boundary layer structure near the air sparger. Various layer heights and cell sizes are created on wall surfaces so that the cells grown in the free stream match up in size/centroid. The particular cell length scales chosen for this work were arrived at through successive meshing of numerical tests. The first grid built is referred to as 1×, and tests were performed to compare 1×, 2×, 4×, and 8× grids. It was found that increased resolution beyond 4× did not change the

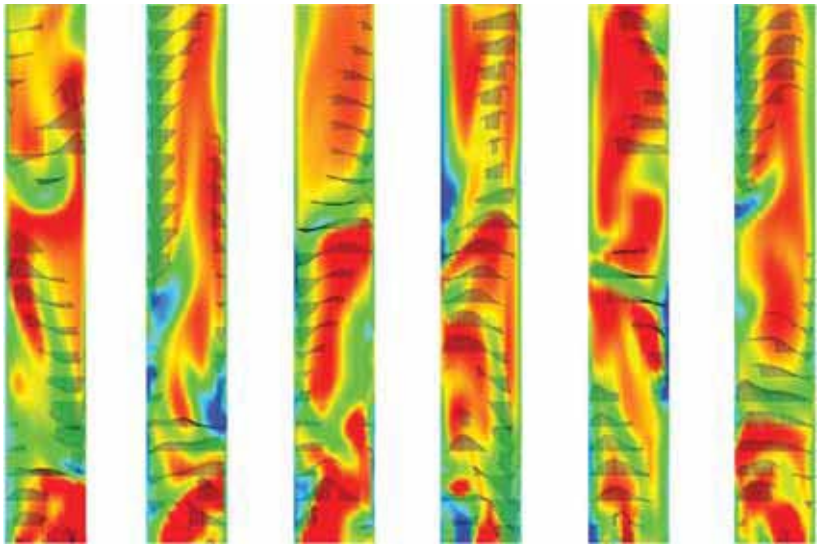

Figure 3. Partial renderings of some uncorrelated instantaneous contour plots of gas volume fraction (red represents high values, while blue represents low values) with superimposed liquid velocity vectors on a column centerline cutting plane.

[Color figure can be viewed in the online issue, which is available at wileyonlinelibrary.com.]

time-averaged radial velocity and gas holdup profiles, so the 4× approach was used for the model results shown in this work.

Convergence

The final mesh is partitioned to run on 8–16 central processing units (CPUs). After months of tuning the model to match reality anchors for a particular geometry and set of operational conditions, a quasi-steady (statistically stationary as discussed in Strasser[39]) solution is sought. Primarily, tuning was needed in the proprietary bubble population balance routines. The model is then run typically for 100 s of bubble column churn time, requiring 2 to 4 weeks of CPU time. The time-step and number of inner loops are chosen such that mass, energy, and each chemical species' mass imbalances are far less than 1% on an instantaneous basis.

Results

Hydrodynamics

With superficial velocities in the range of 0.5–3 m/s, this column operates in well into the heterogeneous flow regime. At this high superficial velocity, Nedeltchev et al.[40] proposes a "coalesced bubble regime (three-region flow)." These three regions are central plume, vortical region, and descending region. The structures meander laterally and circumferentially, in both space and time. Figure 3 shows some uncorrelated instantaneous views on a column mid-plane from one design of this work. These are "partial" renderings in that they do not represent the entire height of the column. The color represents low gas volume fraction (blue) to high gas volume fractions (red), while the black arrows are liquid velocity vectors on that cutting plane. The liquid velocity vectors are not necessarily aligned with the computational mesh. The ranges are purposely not disclosed, but it can be said that the gas volume fraction far exceeds 0.5, while the liquid velocity far exceeds 1 m/s. The locations that show no vectors imply that the flow is aimed into the page and a high likelihood of helical motion. It can be seen that, on average, the flow field does not necessarily represent that which would be expected of the time-averaged flow field (liquid up the center and down near the walls). The flow is violent, constantly shifting up/down, radially inward/outward, and into/out of the page. The phase distribution gets slightly more uniform moving up the column, but, in general, a transition height typical to columns with lower gas velocities is difficult to detect.

Plant validation

It has been proposed that a heterogeneous bubble column is completely specified if three quantities are known, namely overall holdup, radial holdup profile, and energy spectrum.[41] To validate the CFD method, the three quantities are characterized in the CFD model and compared to plant data. Gamma ray tomography scans were taken from the plant to test the first two quantities. The gamma scanning system involved a single movable emitting source on one side of the column and various detectors on the other side. For a known source strength, the strength of the detected beam is a function of the density of the medium between. Of course, baseline (empty column) scans are required to convert radiation intensity into a gas holdup measure. By definition, the results of the gamma scan are time-averaged. Figures 4 and 5 show the axial and radial holdup comparisons. Both plots have been normalized by the volume-averaged gas holdup in the reaction medium. It can be seen that there is a reasonable match between CFD and the plant data. Both show a generally nonsloped axial holdup profile. The overall average of the plant data is lower as the scan was performed at a mildly lower rate than the CFD model was ran. CFD shows a much lower gas holdup down near the sparger than that of the plant. More work is being done to assess the near-sparger

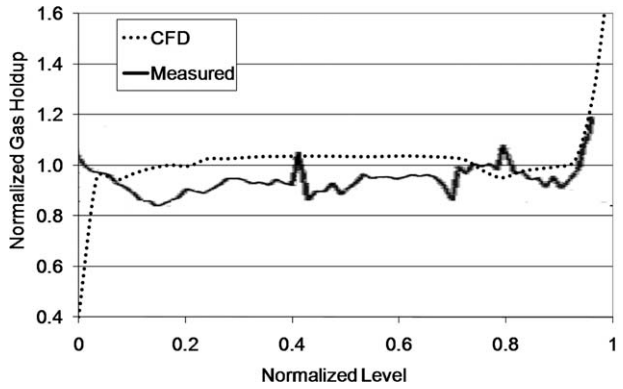

Figure 4. Normalized axial gas volume fraction comparing the model to the plant.

effects. For the energy spectrum, plant data were not available to compare turbulent fluctuating quantities. The closest quantity to this was pressure fluctuations at the lower tangent line, as given in Figures 6 (magnitude) and 7 fast Fourier transform (FFT). Both have been normalized by peak values at the lower tangent line. A strong match is seen between CFD and plant data. The difference between these two sets of results lies in how the data are collected. In CFD, a near-wall point is monitored for temporal static pressure. In the plant, a pressure transducer is connected to the column with a long, small diameter pipe. The intermittent vapor voidage in this small connecting pipeline is expected to attenuate the pressure signal to some extent, and that is precisely what is seen here.

Hydrokinetics

Ideally, a reaction system would have key reactants' availabilities matched with their demands on an instantaneous basis. Reactant concentration samples from various elevations in the numerical column have been compared to plant operating values. There was acceptable agreement for both the time-averaged concentration and the temporal variation. A sample set of random CFD and plant concentration samples of a key reactant are shown in Figure 8. The values have been normalized by the mean. These were taken at uncorrelated times, so they are not expected to match. What we see is a reasonable agreement between the means and the variability. Local concentrations of the liquid and gas phase reactants within the column have a dramatic impact on product quality (see Introduction section). Specifically, low values of a specific gas phase reactant and high values of some liquid phase reactants (as low as 1 ppm by weight) cause the production of color-degrading contaminants. Steady models, that do not include the added effects of fluctuating velocities and fluctuating concentrations, do not detect all of these problematic locations within the column. Problematic concentrations will be referred to as "offensive." Figures 9 and 10 show typical offending gas and liquid phase reactants, respectively, from one design of this work. Again, these "partial" renderings do not represent the entire height of the column. The reader will see "isovolumes," which are depictions of the cells above or below a specified reactant threshold. The colors represent ranges of reactant concentration within the isovolume. For the purposes of the paper, the "offensive" gas phase involves any cell containing less reactant than the time-averaged concentration leaving the column top. That may not necessarily be a threshold for effective oxidizer operation. One will observe that the gas phase reactant is normally offensive down near the gas sparger but can

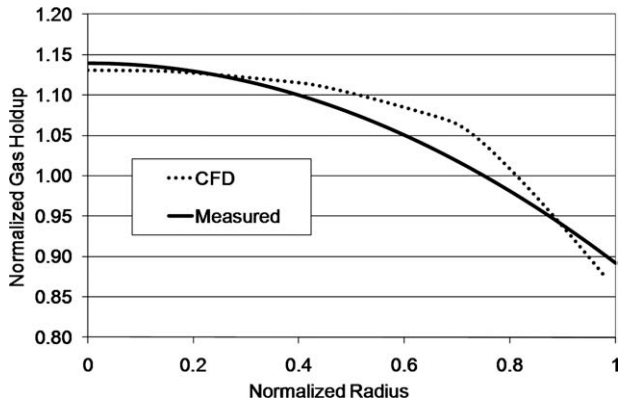

Figure 5. Normalized radial gas volume fraction comparing the model to the plant.

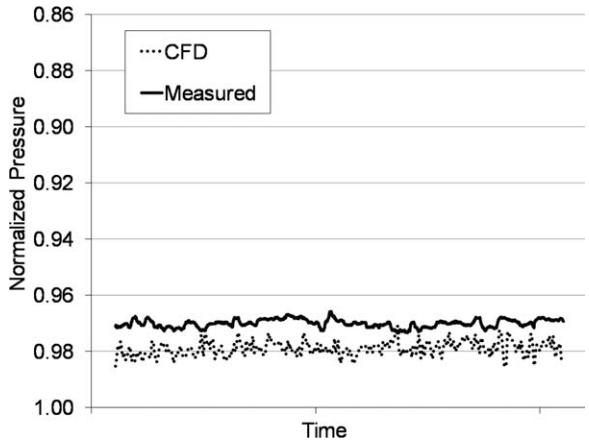

Figure 6. Normalized pressure fluctuations at the lower tangent line comparing the model to the plant.

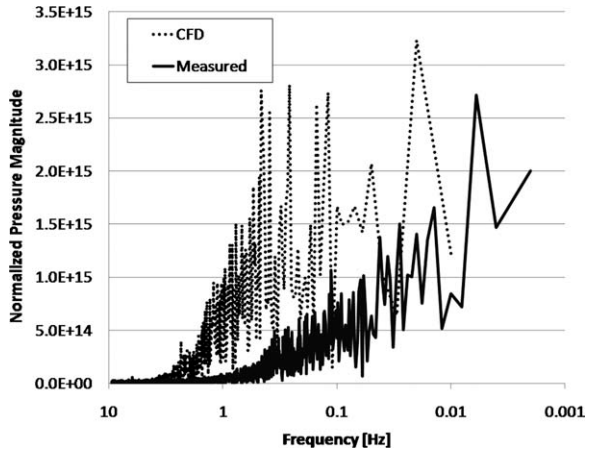

Figure 7. FFT of normalized pressure fluctuations at the lower tangent line comparing the model to the plant.

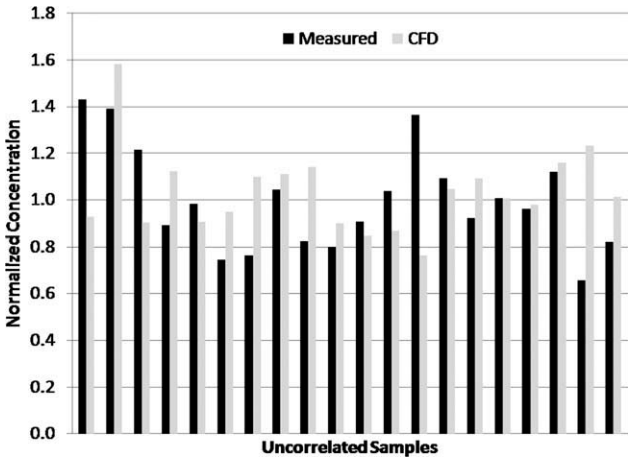

Figure 8. Key liquid phase reactant concentrations taken from a sample port comparing the model to the plant.

Note that these are random, uncorrelated samples. The purpose is to compare the variability in the plant and model.

become offensive anywhere in the column. At some points in time, the total offensive gas phase volume amounts to 30% of the entire reaction mixture volume, while at other times it is as low as 1%. In other words, up to 30% of the reaction volume can contain a gas phase reactant level lower than the value leaving with the gas at the top of the column. The offensive volumes are typically not continuous in space. The offensive liquid phase reactant evolution is equally complex, and the mixture is often offensive near the entry point. At a given sampling time, the volume of offensive liquid phase reactant may or may not be the same shape or total volume as that of the offensive gas phase reactant.

Similarly intriguing results are shown in Figures 11 and 12. Here, we explore mass flow-weighted area-averaged (MFWAA) results at various cutting planes moving from the bottom to the top of the reaction mixture at four different uncorrelated CFD sampling times. Figure 11 involves the gas phase, while Figure 12 involves the liquid phase. For plots of both phases, the concentrations have been normalized to a reference concentration. In general, it can be said that there is a trend from high to lower values progressing up the column. As reactants of both phases are fed closer to the bottom, and as they jointly react, this behavior is expected. Notice that the profiles, local minima and maxima, and the starting and ending values can be dramatically different within normal operation. Again, the instantaneous flow features depart significantly from the time average. An optimized column design must be able to take into account the swings and peaks in both phasic reactants.

As previously discussed, disclosed figures represent results of complex interactions between the spatio-temporal momentum balance, mass transfer effects, and interrelated kinetic relationships. Considering these figures, along with the time-averaged space occupancy of offensive volumes and their locations, the authors have designed an oxidizer that minimizes the offensive zones and produces a higher quality material at a higher rate. Ideally, reactants are ''staged'' properly in that phasic reactants' availabilities match their local reactive needs. This prevents the undesirable, color-forming side reactions from occurring. The authors have found feed methods, feed locations, and column dimensions that meet this goal. For example, liquid phase distribution systems, like that shown in Figure 1, have been incorporated. Two different diameter columns have been modified using our methods. The time-averaged offending volume magnitudes

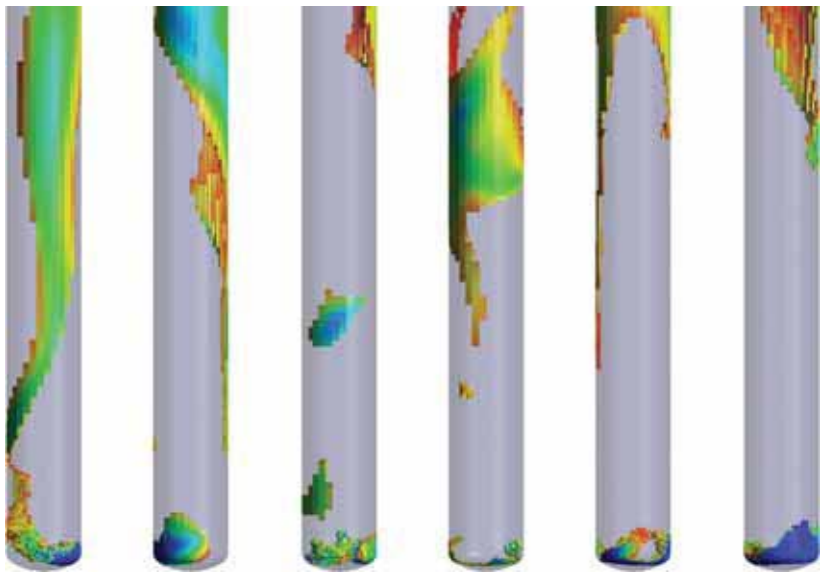

Figure 9. Partial renderings of earmarked offensive gas volumes within the model.

Specifically, these computational volumes contain gas phase reactant concentrations less than the average outlet value. [Color figure can be viewed in the online issue, which is available at wileyonlinelibrary.com.]

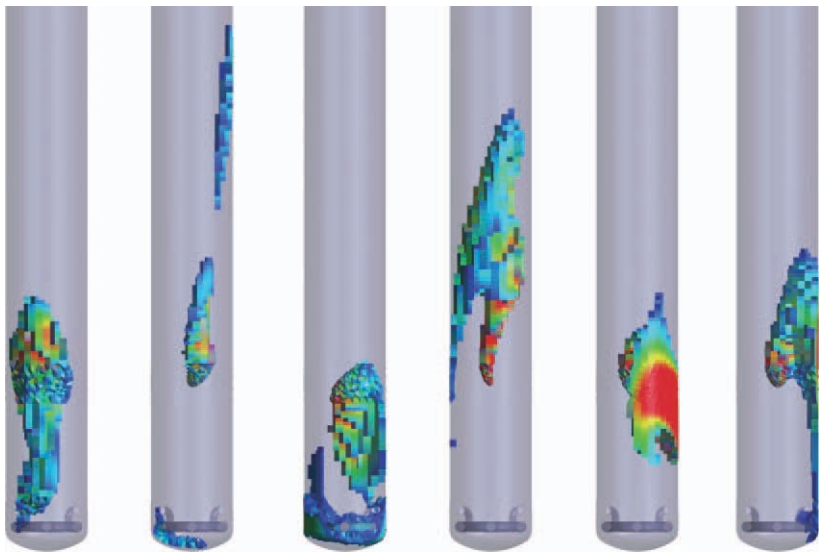

Figure 10. Partial renderings of earmarked offensive liquid volumes within the model.

Specifically, these computational volumes contain liquid phase reactant greater than some predetermined threshold. [Color figure can be viewed in the online issue, which is available at wileyonlinelibrary.com.]

of gas and liquid phase reactants has been reduced by as little as 75% and as much as 95%.

Conclusions

It was desired to study complex, coupled hydrokinetics within a slurry bubble column at highly aerated, high pressure conditions. The open literature for bubble columns is staggering, but nothing apparently exists for the conditions of this work. Steady 3-D compartmental models have been shown in internal evaluations to miss the experimental results; therefore, a transient 3-D Eulerian–Eulerian Reynolds averaged approach was used. The various choices of models and bubble population approach were tuned with grid-independent solutions to match transient and time-averaged experimental information (holdup, pressure fluctuation, and reactant concentrations). After tuning, time-averaged and temporal CFD results from various designs were considered to study methods of improved reactant feeding. The goal is to pair chemical availability with chemical reactivity for various species in each phase, locally throughout the column. Various by-products affect our product's fitness for use differently, while some are important at concentrations as low as 1 ppm by weight. Sample results were displayed for a particular design. Reactant concentrations that were above or below predetermined thresholds were shown; these are responsible for off-quality material or the lowering of production rates. The shape and total volume of the offensive phase material were extremely variable (cumulative volume ranging from 1% to 30% of the total reaction volume) and were typically not continuous in space. Axial profiles of reactants were also shown and proved that there was no apparent typical profile. The local maxima and minima shifted substantially in time. While time averages are useful for making some hydrodynamic CFD vs. experimental comparisons, fluctuating values of the chemical species in each phase are also considered in any optimized commercial design. Said methods have been implemented in

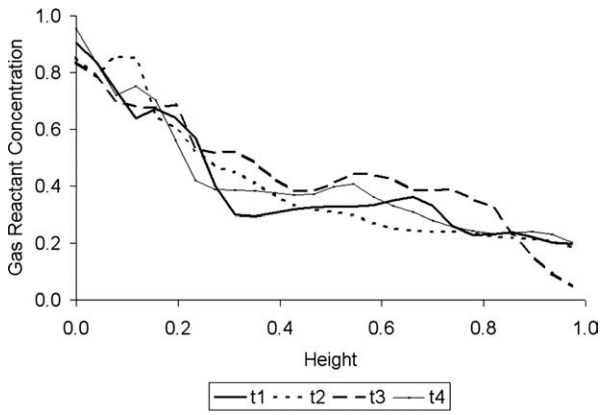

Figure 11. Uncorrelated key gas reactant axial profiles at various instants in time in the model.

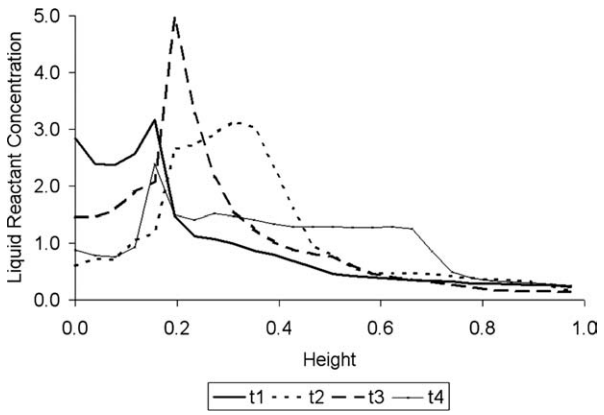

Figure 12. Uncorrelated key liquid reactant axial profiles at various instants in time in the model.

Specifically note the large deviations between sampling times.

designing for large-scale production facilities. For two different diameter columns, offending liquid and gas phase volumes have been reduced by as much as 95%.

Notation

D = diffusivity, m^2/s
g = gravity, m/s^2
k = turbulence kinetic energy, m^2/s^2
k_La = liquid side mass transfer coefficient, s^{-1}
$i - l$ = tensor summation indices
M = momentum source term, $kg/m^2\ s^2$
p = pressure, Pa
r = volume fraction
R = reaction source term, kg/m^3 s
S = source through mass exchange, $kg/m^2\ s^2$
Se = surface coverage parameter from Martin et al.[34]
Sc_t = turbulence Schmidt number
t = time, s
u_g = superficial gas velocity, m/s
u' = fluctuating velocity component, m/s
x = spatial coordinate
α = phase designation
δ = Kronecker delta
ψ = proportionality constant for literature k_La correlations
β = power in literature k_La correlations
ε = turbulence dissipation rate, m^2/s^3
Φ = chemical species
ω = specific dissipation rate, s^{-1}
ρ = density, kg/m^3
μ_t = turbulent (or eddy) viscosity, kg/m s

Literature Cited

1. Nottenkamper R, Steiff A, Weinspach PM. Experimental investigation of hydrodynamics of bubble columns. *Ger Chem Eng*. 1983;6: 147–155.
2. Letzel MH, Schouten JC, van den Bleek CM, Krishna R. Effect of gas density on large-bubble holdup in bubble column reactors. *AIChE J*. 1998;44:2333–2336.
3. Lou X, Lee D, Lau R, Yang G, Fan LS. Maximum stable bubble size and gas holdup in high-pressure slurry bubble columns. *AIChE J*. 1999;45:665–680.
4. Yang G, Lou X, Fan LS. Heat-transfer characteristics in slurry bubble columns at elevated pressures and temperatures. *Ind Eng Chem Res*. 2000;39:2568–2577.
5. Strasser W. Discrete Particle Study of Turbulence Coupling in a Confined Jet Gas-Liquid Separator. *J Fluids Eng*. 2008;130:1–10.
6. Lau R, Peng W, Velazquez-Vargas L, Yang G, Fan LS. Gas–liquid mass transfer in high-pressure bubble columns. *Ind. Eng. Chem. Res*. 2004;43:1302–1311.
7. Jin H, Liu D, Yang S, He G, Guo Z, Tong Z. Experimental study of oxygen mass transfer coefficient in bubble column with high temperature and high pressure. *Chem Eng Technol*. 2004;27:1267–1272.
8. Rosen A, Krylov V. Theory of scaling up and hydrodynamic modeling of industrial mass transfer equipment. *Chem Eng J*. 1974; 7:85–97.
9. Deckwer W, Schumpe A. Improved tools for bubble column reactor design and scale-up. *Chem Eng Sci*. 1993;48:889–911.
10. Zlokarnik M. *Scale-up in Chemical Engineering*. Wiley-VCH, 2002.
11. Martin M, Montes F, Galan M. Physical explanation of the empirical coefficients of gas–liquid mass transfer equations. *Chem Eng Sci*. 2009;64:410–425.
12. Xie G, Li X. An axial dispersion model for evaporating bubble column reactor. *Chin J Chem Eng*. 2004;12:214–220.
13. Rafique M, Chen P, Dudukovic MP. Computational modeling of gas–liquid flow in bubble columns. *Rev Chem Eng*. 2004;20:225–375.
14. Menter FR. Two-equation eddy-viscosity turbulence models for engineering applications. *AIAA J*. 1994;32:1598–1605.
15. Launder BE, Spalding DB. *Mathematical Models of Turbulence*. Academic Press, 1972.
16. Wilcox DC. Multiscale model for turbulent flows. AIAA 24th Aerospace Sciences Meeting. American Institute of Aeronautics and Astronautics, 1986.
17. ANSYS, Inc. CFX Solver Documentation, 2007.
18. Vitankar VS, Dhotre MT, Joshi JB. A low Reynolds number k–ε Model for the prediction of flow pattern and pressure drop in bubble column reactors. *Chem Eng Sci*. 2002;57:3235–3250.
19. Pope S. *Turbulent Flows*. U.K.: Cambridge University Press, 2000.
20. Simonnet M, Gentric C, Olmosa E, Midouxa N. Experimental determination of the Drag coefficient in a swarm of bubbles. *Chem Eng Sci*. 2007;62:858–866.
21. Zhang D, Deen NG, Kuipers JAM. Numerical simulation of the dynamic flow behavior in a bubble column: a study of closures for turbulence and interface forces. *Chem Eng Sci*. 2006;61:7593–7608.
22. Monohan SM, Vitankar VS, Fox RO. CFD predictions for flow-regime transitions in bubble columns. *AIChE J*. 2005;51:1897–1923.
23. Krishna R, Ellenberger J. Gas holdup in bubble column reactors operating in the churn-turbulent flow regime. *AIChE J*. 1996;42: 2627–2634.
24. Ishii M. Two-fluid model based on interfacial area transport equation. 5th International Conference on Multiphase Flow. Paper No. PL4, 2004.
25. Sato Y, Sekoguchi K. Liquid velocity distribution in two-phase bubbly flow. *Int J Multiphase Flow*. 1975;2:79–95.
26. Lopez de Bertodano M. Turbulent bubbly flow in a triangular duct. Ph.D. Thesis. Rensselaer Polytechnic Institute, Troy, New York, 1991.
27. Wilkinson P, Van Schayk A, Spronken J. The influence of gas density and liquid properties on bubble breakup. *Chem Eng Sci*. 1993; 48:1213–1226.
28. Strasser W. Towards the optimization of a pulsatile three-stream coaxial airblast injector. *Int J Multiphase Flow*. In press.
29. Poherecki R, Moniuk W, Zdrojkowski A, Bielski P. Hydrodynamics of pilot plant bubble column under elevated temperature and pressure. *Chem Eng Sci* 2001;56:1167–1174.
30. Prince M, Blanch H. Bubble coalescence and breakup in air-sparged bubble columns. *AIChE J*. 1990;36:1485–1499.
31. Lehr F, Millies M, Mewes D. Bubble size distributions and flow fields in bubble columns. *AIChE J*. 2002;48:2426–2437.
32. Luo H, Svendsen H. Theoretical model for drop and bubble breakup in turbulent dispersions. *AIChE J*. 1996;42:1225–1233.
33. Wang T, Wang J, Jin Y. Population balance model for gas–liquid flows: influence of bubble coalescence and breakup models. *Ind Eng Chem Res*. 2005;44:7540–7549.
34. Martin M, Montes F, Galan M. Theoretical modeling of the effect of surface active species on the mass transfer rates in bubble column reactors. *Chem Eng J*. 2009;155:272–284.
35. Olmos E, Gentric C, Vial C, Wild G, Midoux N. Numerical simulation of multiphase flow in bubble column reactors. Influence of bubble coalescence and break-up. *Chem Eng Sci*. 2001;56:6359–6365.
36. Chen P, Dudukovic MP, Sanyal J. Three dimensional simulation of bubble column flows with bubble coalescence and breakup. *AIChE J*. 2005;51:696–712.
37. Strasser W, Feldman G, Wilkins C, Leylek J. Transonic passage turbine blade tip clearance with scalloped shroud: Part II. Losses with and without scrubbing effects in engine configuration. ASME Paper No. IMECE2004-59116, 2004.
38. Strasser W. CFD investigation of gear pump mixing using deforming/agglomerating mesh. *J Fluids Eng*. 2007;129:476–484.
39. Strasser W. Cyclone-ejector coupling and optimisation. *Progr CFD*. 2010;10:19–31.
40. Nedeltchev S, Shaikh A, Al-Dahhan M. Flow regime identification in a bubble column base on both statistical and chaotic parameters applied to computed tomography data. *Chem Eng Technol*. 2006;29:1054–1060.
41. Shaikh A, Al-Dahhan M. A new methodology for hydrodynamic similarity in bubble columns. *Can J Chem Eng*. 2010;88:503–517.

Manuscript received Oct. 26, 2010, and revision received Mar. 8, 2011.